Submit to: International Journal of Refractory Metals and Hard Materials

Plastic deformation in advanced tungsten-based alloys for fusion applications studied by mechanical testing and TEM

Andrii Dubinko[1], Chao Yin[1,2], Dmitry Terentyev[1], Aleksandr Zinovev[1], Michael Rieth[3], Steffen Antush[3], Monika Vilémová[4], Jiří Matějíček[4], Zhang Tao[5]

[1]Structural Materials Group, Institute of Nuclear Materials Science, SCK·CEN, Mol, 2400, Belgium

[2] Institute of Mechanics, Materials and Civil Engineering, Université Catholique de Louvain, 1348 Louvain-la-Neuve, Belgium

[3] Karlsruhe Institute of Technology, Institute for Applied Materials, 76344 Eggenstein-Leopoldshafen, Germany

[4] Institute of Plasma Physics, The Czech Academy of Sciences, 18200 Prague, Czech Republic

[5] Institute of Solid State Physics, Chinese Academy of Sciences, 230031 Hefei, Anhui, China

Abstract

In this work, we have assessed mechanical properties of several tungsten grades considered as perspective materials for applications in plasma facing components in the nuclear fusion environment, where the neutron irradiation damage is expected to cause embrittlement. In particular, the work focuses on two aspects: bending tests to deduce the onset of ductile deformation and microstructural analysis of the reference and plastically deformed materials. The microstructure in the reference state and the one induced by plastic deformation at 600°C is studied by means of transmission electron microscopy (TEM). Six different types of tungsten-based materials were assessed: two commercial grades produced according to ITER specifications in Europe and China and four lab-scale grades utilizing different reinforcement options. The comparative assessment of tensile and bending strength was performed at 600°C accompanied with a detailed TEM analysis. The deformation-induced microstructure was characterized and compared for all studied grades in terms of the dislocation density, heterogeneity, observation of pile-ups and tangles specifically near grain boundaries and/or strengthening particles. The obtained data will serve as reference information required to assess the impact of neutron irradiation.

Keywords: Tungsten alloys, deformation, plasticity, dislocations

1. Introduction

Development of nuclear fusion electricity production implies a number of technological and scientific challenges, where appropriate selection of materials is one of the major concerns. High temperature operation of materials and components is a must to ensure durable and stable plasma discharge required for the thermal energy generation and extraction to invoke electric energy gain [1]. Thus, refractory metals are naturally considered as main candidates for plasma-facing materials given high thermal conductivity, strength and melting point. The most perspective is tungsten (W) and therefore it is selected as candidate for divertor and first wall material for DEMO [2-4]. One of the critical problems in high temperature applications of refractory metals is mechanical performance in the low-temperature window, where refractory metals exhibit limited ductility due to relatively high ductile to brittle transition temperature (DBTT) 300-400 °C, see e.g. ref. [5] and [6]. Operation of W in ductile mode implies its application above the DBTT i.e. above 300-400 °C. However, upon the operation in fusion environment the DBTT will raise up due to the harsh particle flux, thermal cyclic fatigue and penetration of plasma components [7]. In addition to thermal loads, the irradiation by fast neutrons (14 MeV) will lead to generation of lattice damage across the whole PFC and therefore it may cause brittle failure of tungsten and other materials which are not in direct contact with plasma. This is why the assessment of the neutron irradiation effects in tungsten is especially important at temperatures of 300-600°C, where the irradiation damage should presumably make the material brittle. Physically, the neutron irradiation embrittlement is explained by the formation nano-scale irradiation defects (voids and loops) which obstruct plastic deformation and therefore don’t allow for the ductile blunting of cracks, formed as a result of thermal shocks. Hence, understanding of elementary mechanisms driving plastic deformation, accumulation of stress concentration and eventual failure is important to assess the effect of neutron irradiation and, if understood, possibly propose some mitigation measures to suppress the irradiation embrittlement by specific microstructural or chemical engineering of advanced tungsten grades [8].

Currently, EUROfusion consortium carries a neutron irradiation campaign to investigate the thermo-mechanical properties of industrially available and advanced tungsten grades to assist down selection of different options on the way to develop plasma-facing components sufficiently tolerant to neutron irradiation [9]. The mechanical properties of the commercial tungsten in non-irradiated state, produced by hot rolling/forging (e.g. produced by Plansee and ALMT companies), have been studied earlier in refs. [10-15] including investigation of the effect of texture, annealing and cold-rolling processing. Overall, it is agreed that successful application of W in fusion reactors will be determined by a best compromise between reduced DBTT and enhanced fracture toughness as well as high recrystallization temperature. For that purpose, advanced W-based grades are under development to improve low- and high-temperature performance. For example, particle-reinforced tungsten and reduced grain size material can suppress grain growth, improve strength of grain boundary as well as fracture toughness of the material, and reduce DBTT (see reviews [16, 17]). Fiber-reinforced tungsten allows one to overcome the intrinsic brittleness of tungsten and its susceptibility to embrittlement induced under operation, as W fibers arrest and deflect the propagating cracks (see e.g. [18, 19]). By dedicated alloying with zirconium-carbon (ZrC) nano-sized particles as well as by applying the powder metallurgical process, it was possible to reduce the free oxygen occupying grain boundaries and successfully fabricate bulk plate of W-0.5wt.%ZrC alloy [20]. Preliminary mechanical and high heat flux (HHF) assessment demonstrated that this material exhibits as low DBTT as 100°C and can sufficiently withstand HHF loads up to the power density of 0.66 GW/m^2 [20], simulated by electron beam. Thus the next step is to investigate the impact of the neutron damage. As of now, there is a number of perspective lab-scale tungsten grades with improved mechanical properties whose performance under neutron irradiation is yet to be explored.

This work is dedicated to systematic characterization of bending strength and plasticity of several tungsten grades which are included in the screening irradiation programme. Here, we investigate properties of several materials in a non-irradiated i.e. reference state. The samples are fabricated and tested according to the single specification rule and inspected using the same lab equipment to provide one-to-one comparison. The equivalent sample geometries are used to investigate the effect of neutron irradiation.

This study focuses on mechanical properties of W in the low-temperature application range for PFC (i.e. around 600 °C), where the irradiation induced embrittlement is considered to play a crucial role. The bending and tensile tests are performed at 600 °C. The flexural strain is used as an indicator of the capacity of the material to experience ductile deformation. As proposed by Lassila et al. [21], the ductile-brittle transition temperature (DBTT) is in the range where the flexural bending strain reaches 5%. Using plastically deformed samples, a parametric study of the microstructure is performed by means of transmission electron microscopy (TEM). In particular, the reference microstructure and the one developed in the materials tested at 600°C (deformation to rupture) is investigated in full details including characterization of dislocations, strengthening particles and morphology of sub-grains. The obtained results for mechanical and microstructural properties will serve as reference dataset required to assess the impact of the neutron irradiation effect.

2. Materials and experimental methods

As mentioned above, six types of tungsten material grades were studied in this work. Those were selected following the advance of the European fusion material research programme presented in ref.[22]. Two commercial grades produced in Europe and China according to ITER specification were included as industrial references. These two materials will be referred to as Plansee ITER specification W (IGP) and AT&M ITER specification W (CFETR), respectively. Other four research grades were developed, respectively, by the Karlsruhe Institute of Technology in Germany (particle reinforced tungsten products), by the Institute of Plasma Physics at Czech Republic (spray plasma sintering), and the Institute of Solid State Physics at China (particle strengthening and oxyging soaking by addition of zirconium). These grades are, respectively, W-1 wt% TiC (W1TiC), W-2 wt% Y_2O_3 (W2YO), Fine Grain W (FG), and W-0.5 wt% ZrC (W0.5ZC).

IGP, CEFTR, and W0.5ZC were produced by powder metallurgy and normalized by forging or rolling. The hammering was applied to IGP, while rolling was applied to CFETR and W0.5ZC grades. The latter also passed a specific thermal mechanical treatment (TMT) to reduce the grain size [20]. The two particle reinforced tungsten products (W1TiC and W2YO) were manufactured by powder injection molding (PIM) [23]. Finally, the FG products were manufactured by spark plasma sintering (SPS) processing [24].

2.1 Bending and hardness tests

The three-point bending test set-up was designed following the ASTM E290 standard [25]. The dimensions of the 3PB specimen are 1 mm x 1 mm x 12 mm, which looks similar to a matchstick. The flexural strain (FS%) is calculated using equation (1) as

$$FS\% = \frac{6Dd}{L^2} \tag{1}$$

in which *D* is the maximum deflection of the 3PB specimen, *d* is the thickness of the specimen, and *L* is the supporting span of the test stage (in this case L = 8.5 mm). The loading rate was 0.5 mm/min.

The tests were performed in the environmental furnace at 600°C on a standard INSTRON 3800 universal mechanical testing machine with electrical actuator. The strain was calculated based on the measurements of the pull rod displacement using linear variable differential transformer (LVDT). The LVDT and load cell were calibrated according to the required standards. The samples were cut by electric discharge machine using a wire of 20-50 μm and polished with SiC paper of 2000 grit size.

Hardness of the materials was measured by Vickers micro-hardness tests. Micro-hardness measurements were performed with Struers DuraScan 50 Vickers hardness tester machine controlled via external PC, using ecos Workflow software for automated measurements and calculations. The Vickers hardness was measured in range of 0.025 to 2 kg load force, however, here we provide the results of the measurements done at 0.2 kg, as this load force will be available for the neutron irradiated materials in our upcoming post irradiation campaign.

2.2 Tensile plastic deformation

To perform tensile plastic deformation experiments flat mini tensile samples of dog-bone shape were cut from the pristine material. The gauge sections dimensions were 5.2×1.5×1.6 mm, thus the tensile cross-section was 2.4 mm^2. The mechanical tests were conducted in air at 600°C applying a deformation rate of 0.2 mm/min, corresponding to the strain rate of 6.4 x 10^{-4} s^{-1}. The results of those mechanical tests are presented and discussed in our earlier paper [26]. Post deformation study by SEM has shown that the oxidation at 600°C within the test time was not significant and the top surface (i.e. several microns) was removed during the standard procedure of sample preparation to perform sub-sequent TEM analysis.

2.3 TEM measurements

After the above described tensile plastic deformation, the broken mini tensile samples were cut into pieces with a size of about 1.5x1.5x1.6 mm to perform TEM analysis. In all cases, the samples were cut from the necking region to provide the analysis of the region experienced largest plastic deformation.

The pieces for TEM samples were mechanically polished from both sides using SiC paper with grit sizes of 220, 500, 1200, 2000 and 4000 to achieve 70-100 μm thickness and further cut with a wire cutter into pieces to fit 3 mm TEM grids. They were polished again from both sides with 4000 SiC paper to remove the remnants of glue, rinsed in ethanol and then glued on 3 mm copper grids with an aperture of 1 mm. Finally, TEM specimens were polished electrochemically with a solution of 1.5 wt.% NaOH in water with applied voltage of 30 V. The specimens were investigated with JEOL 3010 TEM operating at 300 kV. The TEM images were taken using bright condition to enhance resolution of dislocation lines in bulk and those forming grain boundaries, as these were the primary objects for this investigation. The average dislocation density was measured following the methodology used in [27]. Each calculation requires a TEM micrograph, corresponding diffraction pattern and a convergent beam electron diffraction (CBED) pattern. In Digital Micrograph software, provided with the image sensor of a microscope, a circle is drawn randomly in an image and the number of intersections of it with dislocation lines is counted. Dislocation density is then calculated as $\rho=2N/Lt$, where N is the number of intersections of the circle with dislocation lines, L – length of the circle, t – local thickness of the specimen at the area of the image. The length of the circle is automatically calculated in the Digital Micrograph software. The local thickness of the specimen is determined from the CBED pattern and diffraction pattern. Several calculations at different areas of the specimen were performed to get an average number of dislocation density.

Scanning electron microscopy (SEM) measurements to assess the grain size and morphology were carried out using a FEI instrument. The specimens were cut from the raw material in disk form and were subsequently mechanically polished, electropolished at 20 V in a 4% aqueous solution of NaOH and finally etched at 3 V using an etchant consisting of 25 cc of a normal solution of NaOH and 20 cc of H_2O_2.

3. Results

3.1 Reference grain microstructure and mechanical properties

The microstructure of grains, as was studied in our earlier work [26], is presented as Inverse Pole Figures mapped by Bruker Quantax software in Fig.1. The nominal chemical composition and effective grain size, as determined by the Quantax software, are provided in Table 1. As one can see, the IGP and CFETR clearly exhibit the texture and elongated grains aligned with the rolling direction (LD). IGP consists of carrot-like grains, while CFETR has pancake-like grain structure. The grain elongation is less pronounced in W0.5ZrC but still present there. W0.5ZrC is supplied as a rolled plate. FG and PIM materials exhibit uniformly shaped grains, separated mostly by high angle grain boundary interfaces, as one would expect given that the sintering was performed at high temperature.

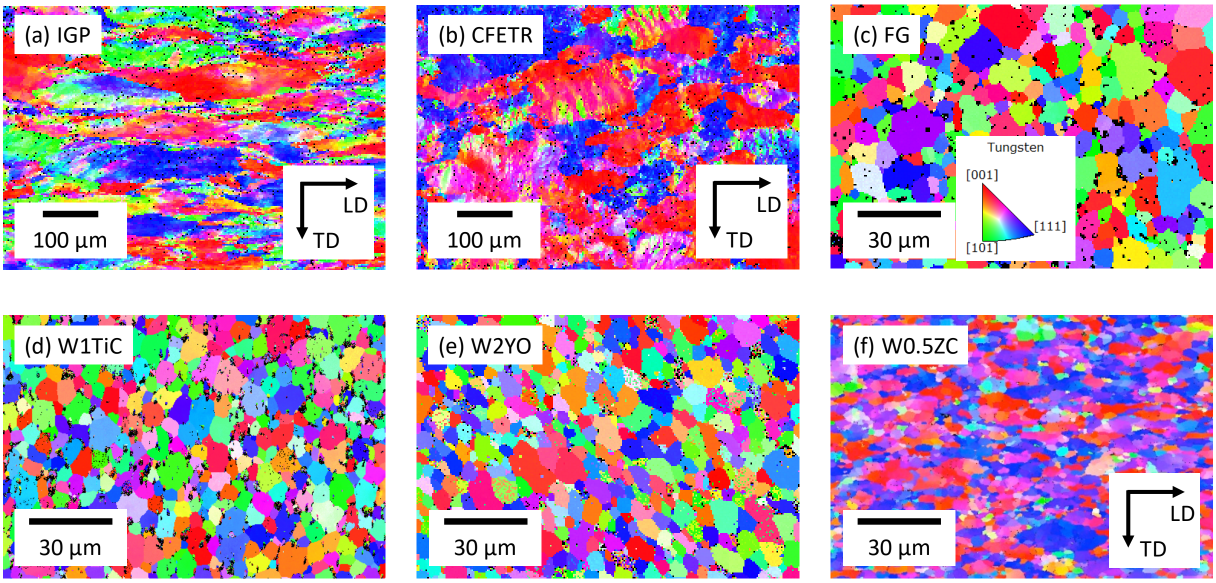

Fig.1. SEM maps of studied materials. Normal direction (ND) Inverse pole figure (IPF) of baseline and advanced W: (a) IGP; (b) CEFTR; (c) FG; (d) W1TiC; (e) W2YO; and (f) W0.5ZC. Colour code refers to the orientation of grains. LD and TD refer to longitudinal and transverse directions respectively.

Table 1. Chemical composition and grain characteristics of the studied tungsten grades.

Materials	IGP	CEFTR	FG	W1TiC	W2YO	W0.5ZC
Composition	Pure W (> 99.97 wt%)	Pure W (> 99.94 wt%)	Pure W (> 99.7 wt%)	99 wt% W + 1 wt% TiC	98 wt% W + 2 wt% Y_2O_3	99.5 wt% W + 0.5 wt% ZrC
Equivalent Medium Diameter (μm)	87.44	60.28	9.36	7.76	7.32	6.66

Fig.2 presents a summary of tensile properties obtained at 600°C: (a) stress-strain curves, (c) tensile strength properties and (c) uniform elongation together with the initial dislocation density (as measured by TEM, see techniques in the sub-section 2.3). The results of the three-point bending tests, performed at 600°C, are presented in Fig.3. Let us summarize the mechanical response of the studied grades at 600°C.

- commercial tungsten produced in a shape of a rod (Plansee, Austria - IGP) and a plate (AT&M, China - CFETR) shows rather high yield point, 470-540 MPa, where AT&M product has a slightly higher strength, see Fig.2(a). For both L- and T-orientations the uniform elongation is practically zero and the materials exhibit essentially early necking formation. The early necking is determined by relatively high initial dislocation density (~5×10^{12} m^{-2}, see Fig.6c) and small sub-grain size (discussed in the next section). However, the ductile necking deformation is considerable and the true fracture stress (i.e. product of engineering stress at fracture and strain at fracture) is the highest among all tested grades, see Fig.2(b), exceeding 1 GPa. The $\sigma_{0.2}$/HV0.2 ratio is about 1.03-1.06 for this material.
- SPS-produced grade, referred to as FM, exhibits the lowest yield stress among the tested materials. The material exhibits uniformly shaped grains of 10-20 μm size and rather low initial dislocation density, see Fig.2(c). This explains rather low yield stress and quite high uniform elongation. Note that the true fracture stress of the FM grade (180 MPa) is comparable to the one of PIM and W0.5ZrC materials but a factor of five smaller if compared to the commercially pure W grades.
- PIM grades exhibit similar microstructural and mechanical characteristics as FM grade, however, the yield stress is somewhat higher due to a smaller grain size. The true fracture stress for W2YO grade is only 52 MPa, which is the lowest value among the all. The true fracture stress of W-1TiC is comparable to the FG and W0.5ZrC grade, being 215 MPa. It is interesting to note that the $\sigma_{0.2}$/HV0.2 ratio for FP and PIM grades is about 0.8-0.86, which is considerably lower the one measured for commercially pure W and W0.5ZrC grades. In general, PIM grades are characterized by considerable uniform elongation and high work hardening rate, which is defined by the structure of grain boundaries and strengthening particles which apparently effectively pin dislocations causing their quick multiplication.
- ZrC strengthened grade is characterized by the highest yield stress (see Fig.2a) and smallest grain size (see Fig.1). An excessively high value of the yield strength is achieved also thanks to high initial dislocation density (see Fig.2c). At 600°C, the material deforms in a similar mode as commercially pure W i.e. by early necking. However, the total elongation of W0.5ZrC is lower compared to commercially pure W, and this is apparently why the true fracture stress is also much lower, being comparable to that of PIM and FG grades.

By comparing bending and tensile response (i.e. comparing Fig.2a and b), we can clearly see the correspondence of the mechanical properties. In particular, the order at which the flexural strength at

0.2% of flexural strain appears for the different materials is exactly the same as $\sigma_{0.2}$ found from the tensile tests. The capacity for the work hardening is also seen from the 3PB tests for the PIM and FG materials, which is fully consistent with the results from tensile tests. This is quite an important observation as it allows us to rely on the bending properties as a proxy to deduce tensile yield strength and up to some extend to evaluate the work-hardening capacity.

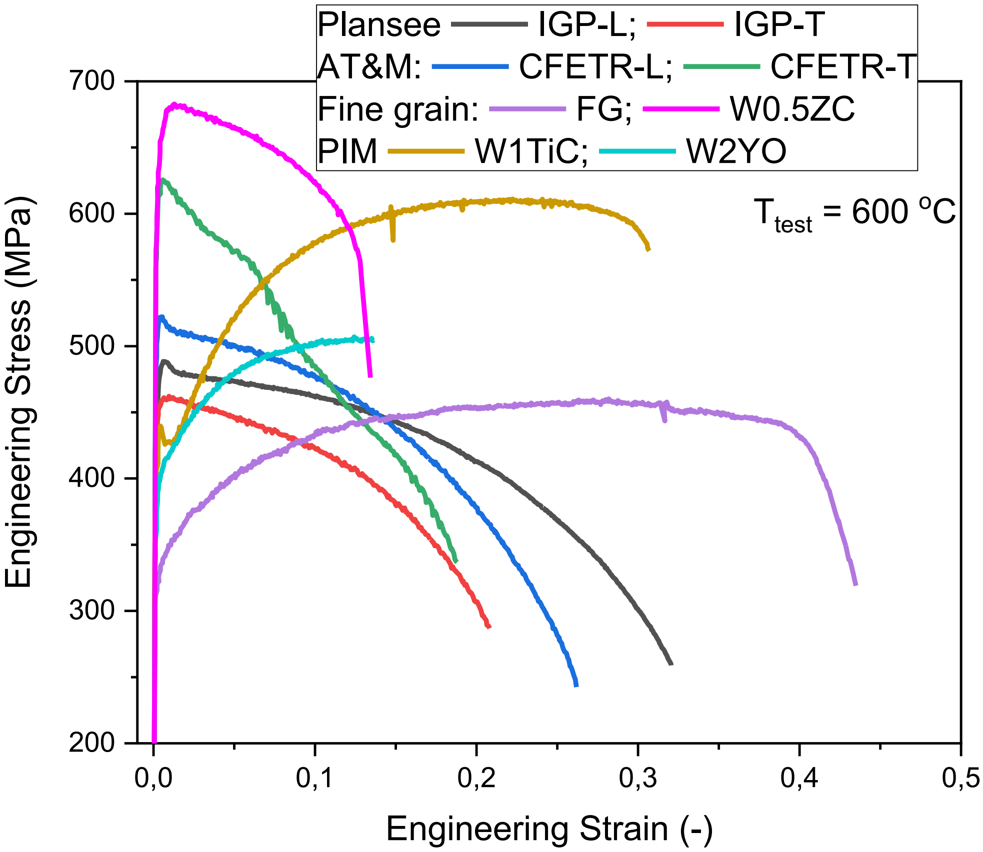

(a)

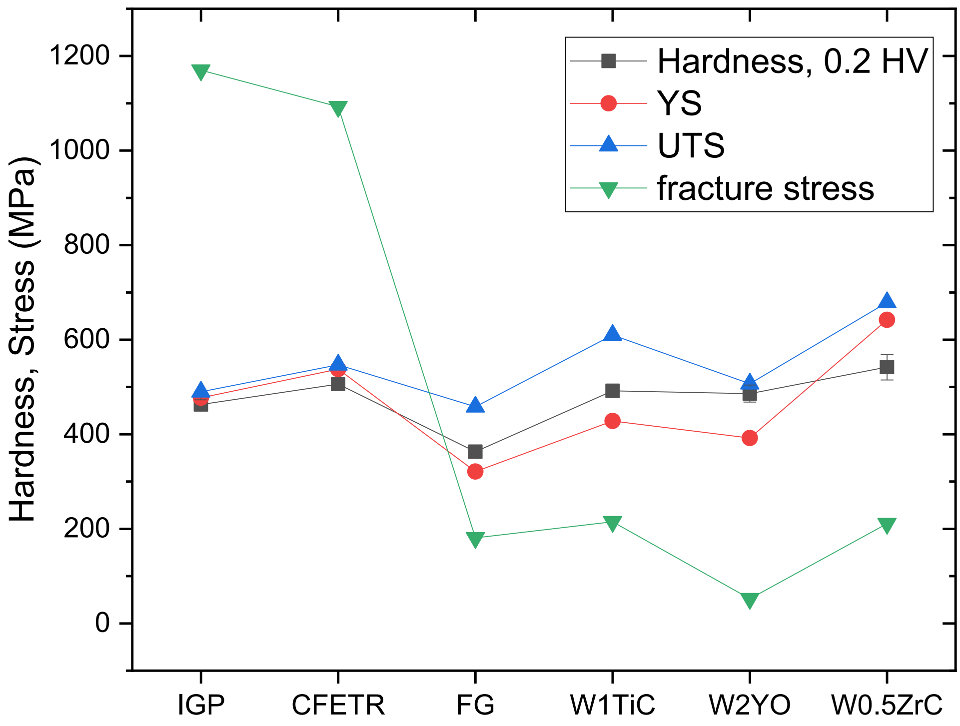

Hardness, Stress (MPa)
1200
1000
800
600
400
200
0
IGP
CFETR
FG
W1TiC
W2YO
W0.5ZrC
Hardness, 0.2 HV
YS
UTS
fracture stress

(b)

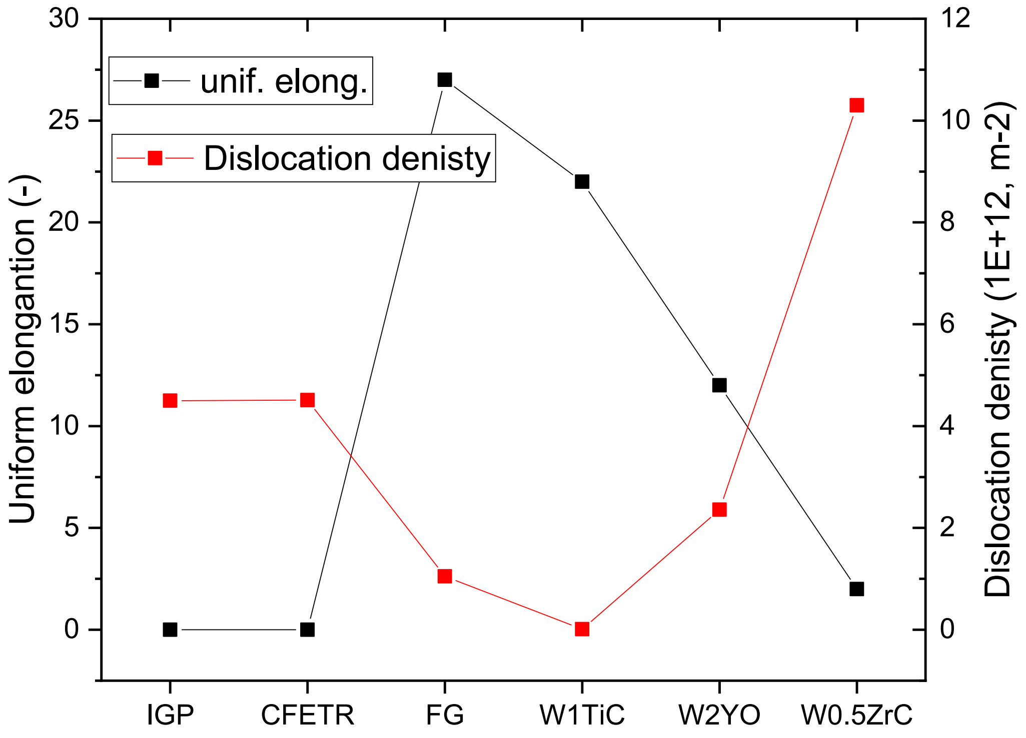

(c)

Fig.2 (a) Engineering stress-strain curves of tungsten grades; (b) summary of tensile strength properties at 600°C ($\sigma_{0.2}$, UTS, fracture stress). UTS and $\sigma_{0.2}$ are provided for the longitudinal orientation of the samples; (c) uniform elongation (for the longitudinal orientation of the samples) and initial dislocation density.

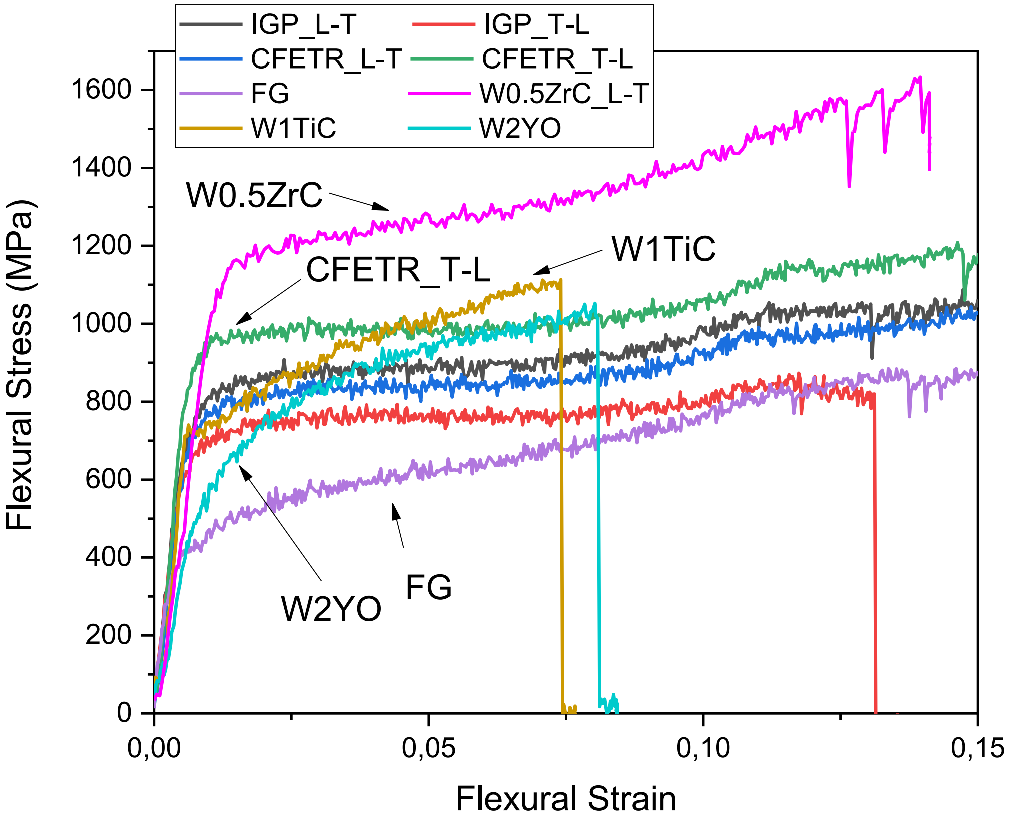

Fig.3 Flexural stress vs. flexural strain obtained at 600°C.

3.2 Reference TEM microstructure

Prior to proceeding with presenting and discussing the results, it is important to note that fabricating TEM samples after plastic deformation from the gauge section of the tensile samples was not straightforward for all tested materials. For some of the materials, especially PIM and FG grades, which exhibited large work hardening, the preparation of samples after plastic deformation was challenging due to brittle nature of the deformed tungsten. As a result, only limited surface was thin enough to be transparent for the electron beam

Fig.4 shows the composite image (which is composed of 10-20 TEM images stitched together to show an overview of several sub-grains) of the microstructure resolved in (a) IGP and (b) CFETR materials in the reference condition. TEM measurements show elongated sub-grains, the elongation direction coincides with the rolling direction. In the case of the IGP material, the size of sub-grains varies in the range 0.6 – 1.7 µm and 2.3 – 4 µm, respectively, normal to and along the elongation directions. Similar variation of the sub-grain size is registered for the CFETR material. The dislocation density is in the range (4-8)×10^{12} m^{-2}, depending on particular sub-grain, and is being 4.5×10^{12} m^{-2} on average for both grades. More details about the reference microstructure of the IGP and CFETR samples can be found in our earlier works [28, 29].

Low magnification images of the PIM tungsten grades strengthened by TiC and Y_2O_3 particles are shown in Fig.5(a) and (b), respectively. In the case of the precipitate-strengthened tungsten, the control of the local thickness during the sample preparation by electro-chemical polishing was very complicated (due to the different rates of chemical erosion of W and precipitates), which is why it was not possible to obtain large overview sections such as was done for the commercially pure W grades. In both PIM grades, besides the precipitates, triple junctions and well-defined straight grain boundary interfaces were observed. The observation of dislocation lines present inside grains was very scarce. In the case of W1TiC (Fig.5a), not a single dislocation line was observed after inspecting an area of about 70 μm^2, which provides an upper estimate of the dislocation density to be 10^{11} m^{-2}. TiC precipitates had a size of 1-3 µm, which is consistent with the spots of un-resolved regions on the SEM-EBSD images. The size of Y_2O_3 precipitates was up to 1-1.5 µm, and contrary to the W1TiC material, much smaller (also non-coherent) precipitates of size ranging from 50 to 100 nm were observed by TEM. Identification of those precipitates on the SEM-EBSD maps is not straightforward. Major fraction of Y_2O_3 precipitates was attached to the grain boundary or located at the triple junction directly, see Fig.5(b). Dislocation lines were regularly seen inside the grains in W2YO and their average density is evaluated as 2.36×10^{12} m^{-2}.

As in the case of the PIM materials, obtaining large overview area was difficult due to the presence of pores in the FG grade and due to the presence of high density of ZrC precipitates in the W0.5ZrC grade. Bright field TEM images for these grades are provided in Fig.7 (a) and (b and c). FG W microstructure consists mostly of well-defined high angle grain boundaries and triple junctions, see Fig.7(a). Most of the dislocation lines observed had a straight-line shape and the dislocation lines were always attached to straight (and therefore rigid) grain boundary interfaces. The mean dislocation density is 1.05×10^{12} m^{-2}, which is the lowest value reported here, given that no dislocation lines were observed in the W-1TiC material (and the uppermost dislocation density could only be evaluated on the basis of the inspected surface). No sub-grains were observed in the FG tungsten. The microstructure of the W0.5ZrC material is exhibits high density of small ZrC precipitates. The precipitates are roughly spherical in shape and their size is in the range 100-200 nm. Rarely, the precipitates with a size up to 0.5 µm are observed. Fig.6(b) shows a lower magnification images from which one may get an impression that the precipitates are distributed purely homogeneously over the observed area. However, by inspecting the precipitates at high magnification, see Fig.6(c), one can see that many of precipitates are interconnected with each other by grain boundary interfaces thus forming a sort of honeycomb network, which is also consistent with the SEM-EBSD images (if seen at high magnification). The observation of dislocations and the measurement of their density requires application of high magnification, as otherwise dislocation objects cannot be resolved. Most of the dislocations are observed as tangles and networks, see Fig.6(d), which is a sign of hot deformation applied to fabricate the plate. The average dislocation density reaches 1.03×10^{13} m^{-2}, which is the highest initial dislocation density among the studied materials.

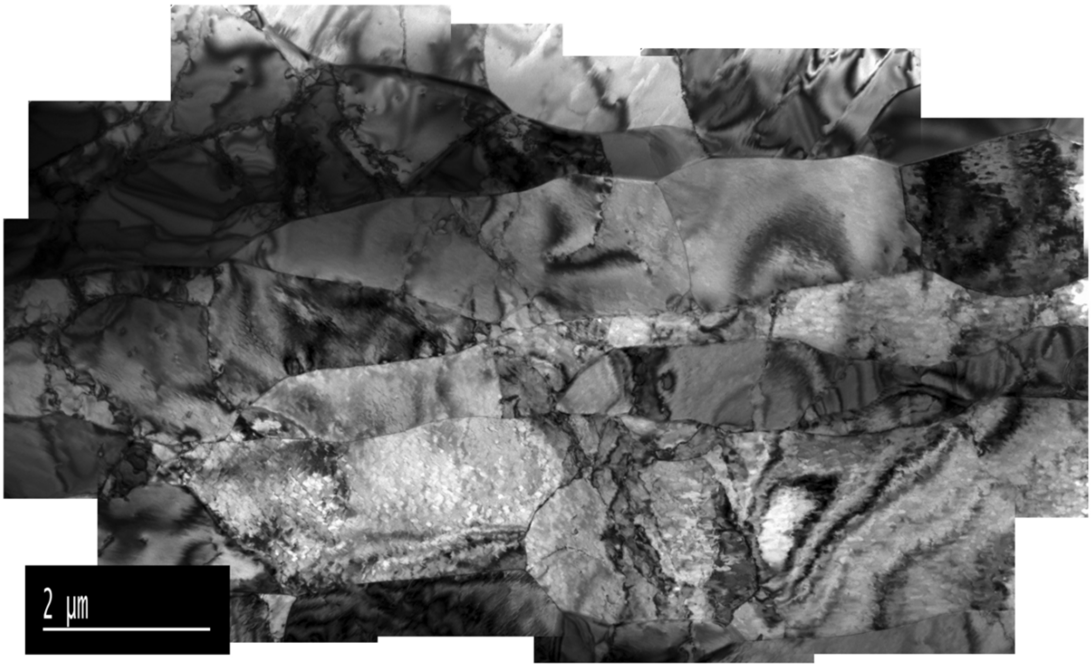

(a)

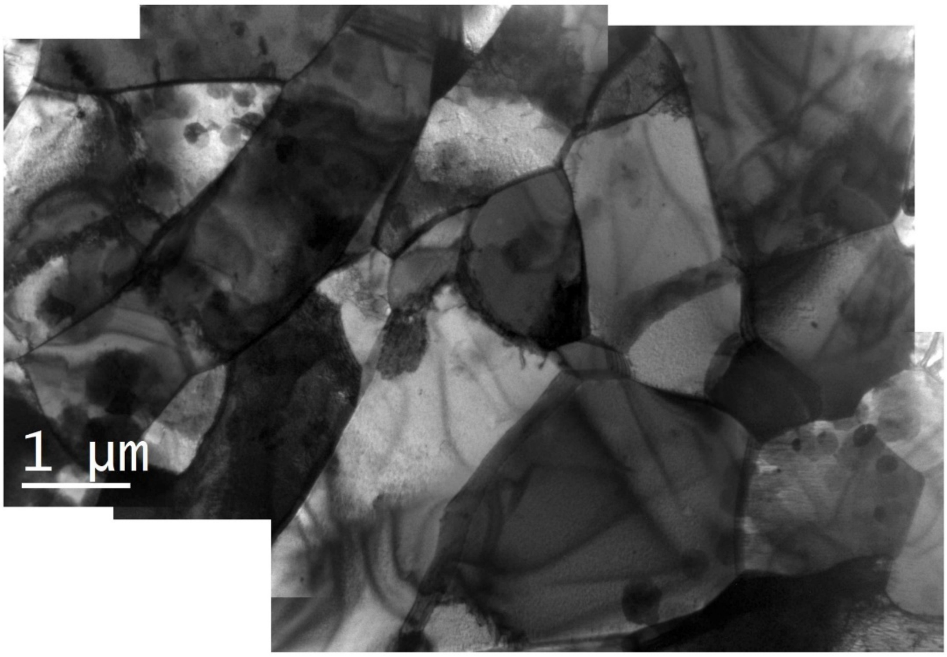

(b)

Fig.4. A composite TEM micrograph of the typical bulk microstructure of (a) IGP and (b) CFETR in the as-received condition, see text for details.

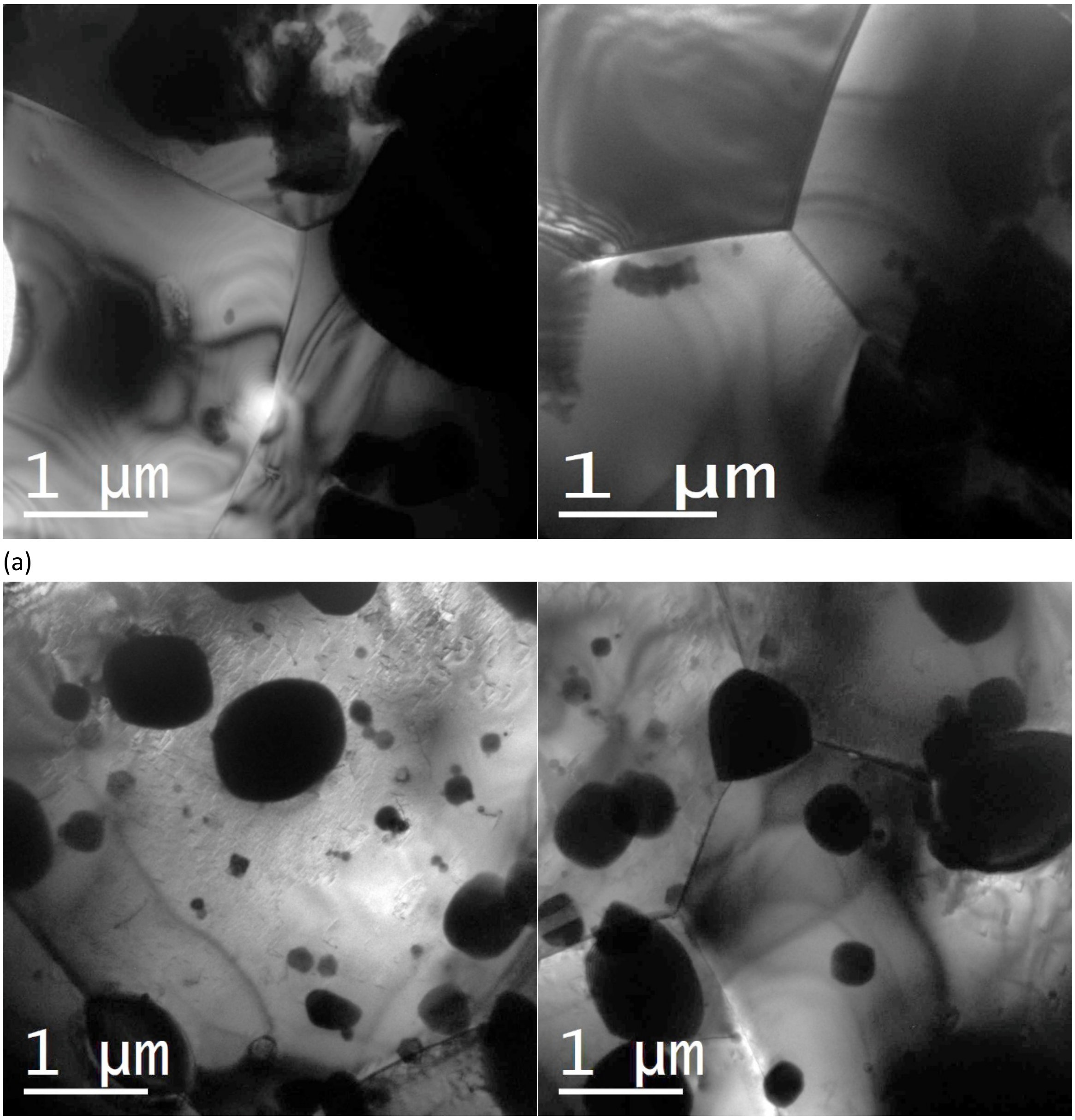

(a)

(b)

Fig.5. Low magnification TEM micrographs of the typical bulk microstructure of (a) W1TiC and (b) W2YO in the as-received condition, see text for details.

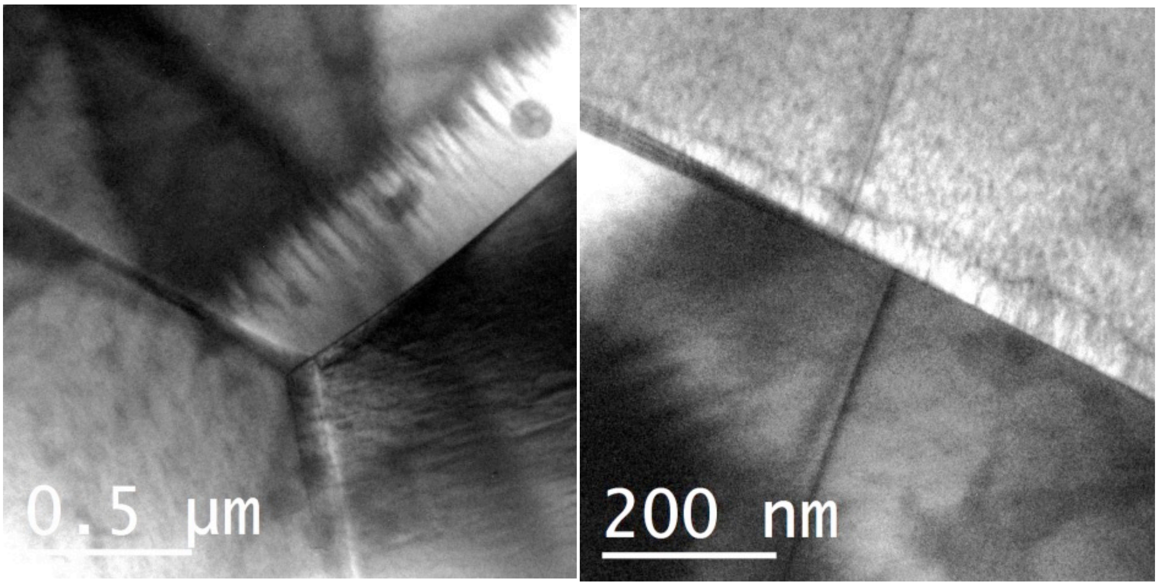

(a)

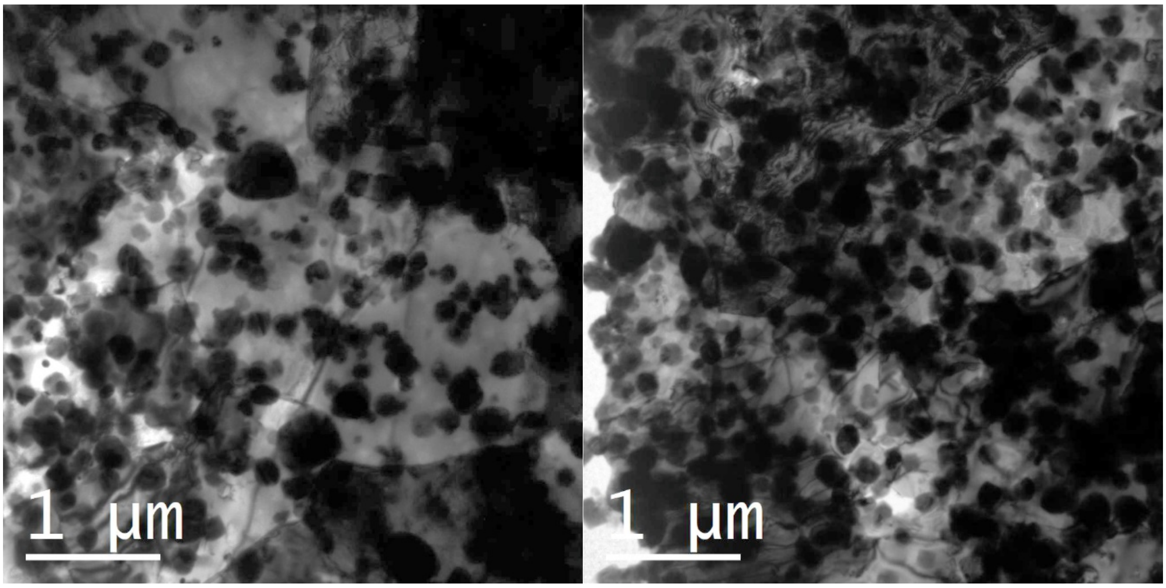

(b)

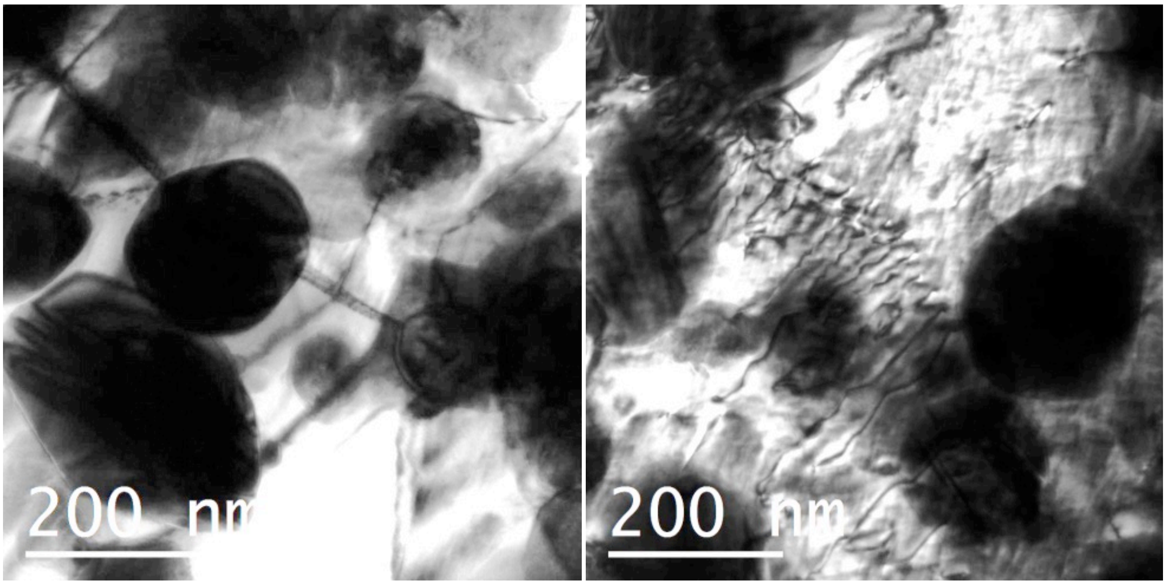

(c)

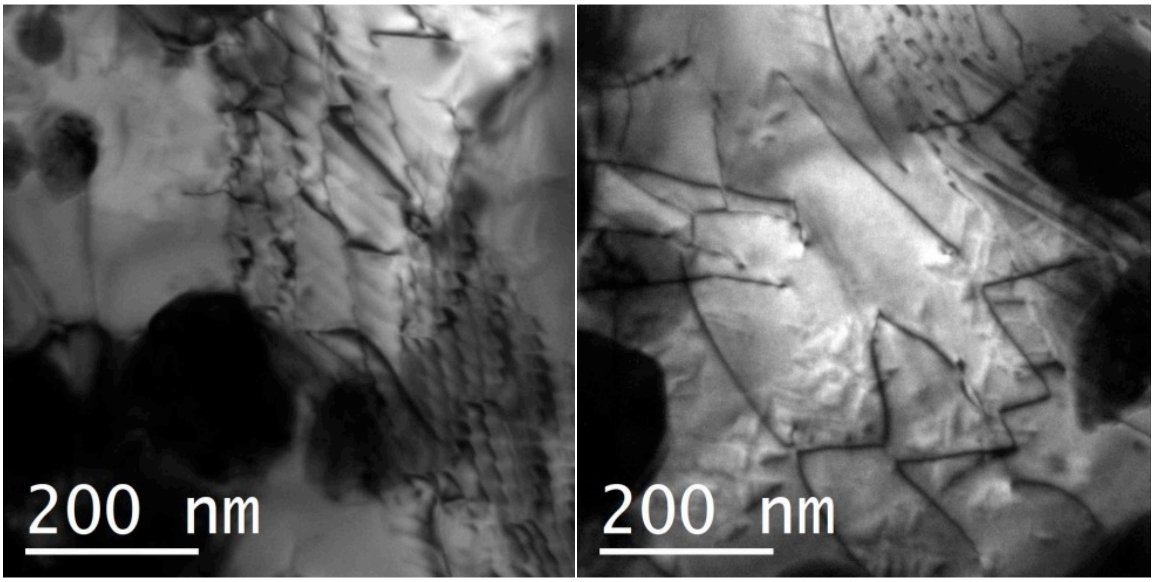

(d)

Fig.6. Low magnification TEM micrographs of the typical bulk microstructure of (a) FG and (b) W0.5ZrC in the as-received condition, see text for details. (c,d) High magnification TEM micrographs of W0.5ZrC showing the appearance of dislocations in the as-received condition.

3.3 TEM microstructure in as-deformed samples

TEM images of the microstructure obtained after plastic deformation in IGP, CFETR, WTiC, W2YO, FG and W0.5ZrC are presented, respectively, on Figs. 7-14.

The microstructure of plastically deformed IGP (Fig.7,8) and CFETR (Fig.9) turned out to be very similar, hence, we will discuss the details on the example of the IGP material. In both deformed materials we see an increase of dislocation density – to 1.02×10^{14} m^{-2} and 2.07×10^{13} m^{-2} in IGP and CFETR respectively. Fig.8 presents several high magnification images of microstructure obtained from the necked part of the IGP sample ruptured at 600°C in the uniaxial test. The images, provided in Fig.8, are taken to show several specific features of the plastic deformation applied. In all shown images, the increase of the dislocation density is obvious. A closer look at the sub-grain boundary interfaces (Fig.8a and b) reveals that a significant accumulation of dislocations and formation of dislocation pile-ups took place there, and some of them start to take a sort of band-like structure. The broadening of the sub-grain interfaces, in some places up to 100-200 nm, is evident on those figures as well as the formation of dislocation pile-ups near the low-angle grain boundaries. In addition, there are many sub-grains where there is a high dislocation density (up to 10^{15} m^{-2}) in the interior of the subgrain (e.g. see Fig.8c). At the same time, some of the regions with high dislocation density, tangles and networks are bridged with the regions being free of dislocation lines. This creates a large local fluctuation in the assessment of the dislocation density, however, the increase of the mean value is undoubtful. The size of the sub-grains did not change much compared to the non-deformed material, however, grain boundaries became much “wider” which effectively reduced the subgrain interior area.

Finally, we need to notice that some dislocation loops (with typical sizes in a range of 7-13 and 5-20 nm) were also observed in IGP and CFETR respectively. We did not perform rigorous analysis of the loops, but these loops are expected to form as a result of dislocation-dislocation interaction. The loops were not seen before the plastic deformation. As a summary of TEM observations for IGP and CFETR, we can conclude that the plastic deformation caused rather strong heterogeneity in the spatial dislocation density distribution. Apparently, plastic deformation was conducted by the dislocation tangling and formation of pile-ups near grain boundary interfaces. No clear deformation channels were observed (see e.g. Fig.9), which means that plastic deformation was controlled by pinning of dislocations by grain boundaries, which remain sufficiently strong to prevent transmission of pile-ups, which otherwise would lead to the presence of deformation bands.

Fig.10 and Fig.11 present the microstructure of the deformed PIM materials, W1TiC and W2YO grades, respectively. These two materials also have very similar patterns of plastic deformation. The rupture of the tensile samples occurred shortly after the UTS, which means that the post necking deformation was rather limited. Preparation of the samples from the gauge section was the most complicated for these two materials (and FG grade as well) due to the presence of the precipitates (and cavities in the FG grade). Unfortunately, we could not get a large view composite image as in the case of IGP and CFETR material.

Fig.10 shows a typical microstructure of 10 μm^2 of W1TiC grade after the deformation. Clearly, the deformation induced many dislocation lines present in the interior of grains as well as damaged the grain boundary interfaces which were perfectly linear in the reference sample. A higher dislocation density and tangles are usually observed nearby the TiC precipitates.

The overview image for W2YO is given in Fig.11a, which provides the same observations as listed for W-1TiC sample. On Fig. 11b, a high magnification images show the region with low dislocation density in the grain interior (left image), high density near the grain boundary (middle image), and dislocation network which expands within the grain (on the right image). Differently from W1TiC where most of the TiC precipitates were mostly observed at triple junctions, Y_2O_3 precipitates are located at both grain boundaries and inside grain interiors. Near some of the Y_2O_3 precipitates we could clearly observe the formation of tangles, while some remain free of any dislocations. Fig.11c shows the high magnification images of the region containing Y_2O_3 precipitate near dislocation tangles in the left image.

The presence of Y_2O_3 precipitates isolated from the dislocation tangles/networks is shown in the middle image of Fig.11c. Dislocation loops (ranging between 7 to 17 nm in size) were also observed in these materials after plastic deformation. Examples of dislocation loops can be seen in the right image of Fig.11c.

The microstructure of the FG grade after the tensile deformation is presented in Fig.12. The deformation has induced strong increase of the dislocation density to 5.15E+13 m-2. The newly created dislocation lines are distributed within grains forming tangles and networks, as well as intensive formation of the pile-ups is seen near grain boundaries. As in the case of the PIM materials, the pattern of initially straight and rigid grain boundaries becomes widened and curved after the plastic deformation. This points to the fact that the structure of the grain boundaries is damaged by the plastic deformation as well as to the fact that grain boundaries are acting as main features controlling plastic deformation. No signature of the deformation bands or dislocation-free channels is seen.

Finally, a composite TEM image of W0.5ZrC material is presented in Fig.13, while particular features of the plastic deformation are provided in Fig.14. Overall, the deformation induced relatively uniform changes in the microstructure. Grain and sub-grains are elongated in the direction of the application of tensile force. Fig.14(a) shows a magnification image of elongated sub-grains. As a result of the deformation, grain boundaries exhibit significant broadening as shown in Fig.14(b). The density of dislocations has increased on average from 10^{13} up to 5×10^{13} m^{-2}. However, not so many tangles and pile-ups, as it was seen in the PIM and FG grades, were observed in the W0.5ZrC. An example of typical appearance of dislocation lines within a single sub-grain is given in Fig.14(c). As one can see, the dislocation lines homogeneously populate an interior of the sub-grain. Neither did we observe intensive pile-ups near the ZrC precipitates. An example of the precipitate embedded in the sub-grain and surrounded few several pinned dislocations is shown in Fig.14(d). Dislocation loops after plastic deformation were also found in this material. An example of such a loop is shown in Fig.14(d).

It is to be noted that the density of the loops observed in IGP, CFETR, W2YO, W0.5ZrC is in the range of 10^{18} m^{-3} – 10^{19} m^{-3}, which is much lower compared to a typical density of the loops observed after neutron irradiation (being 10^{20} m^{-3} – 10^{22} m^{-3}, depending on irradiation temperature and fluence).

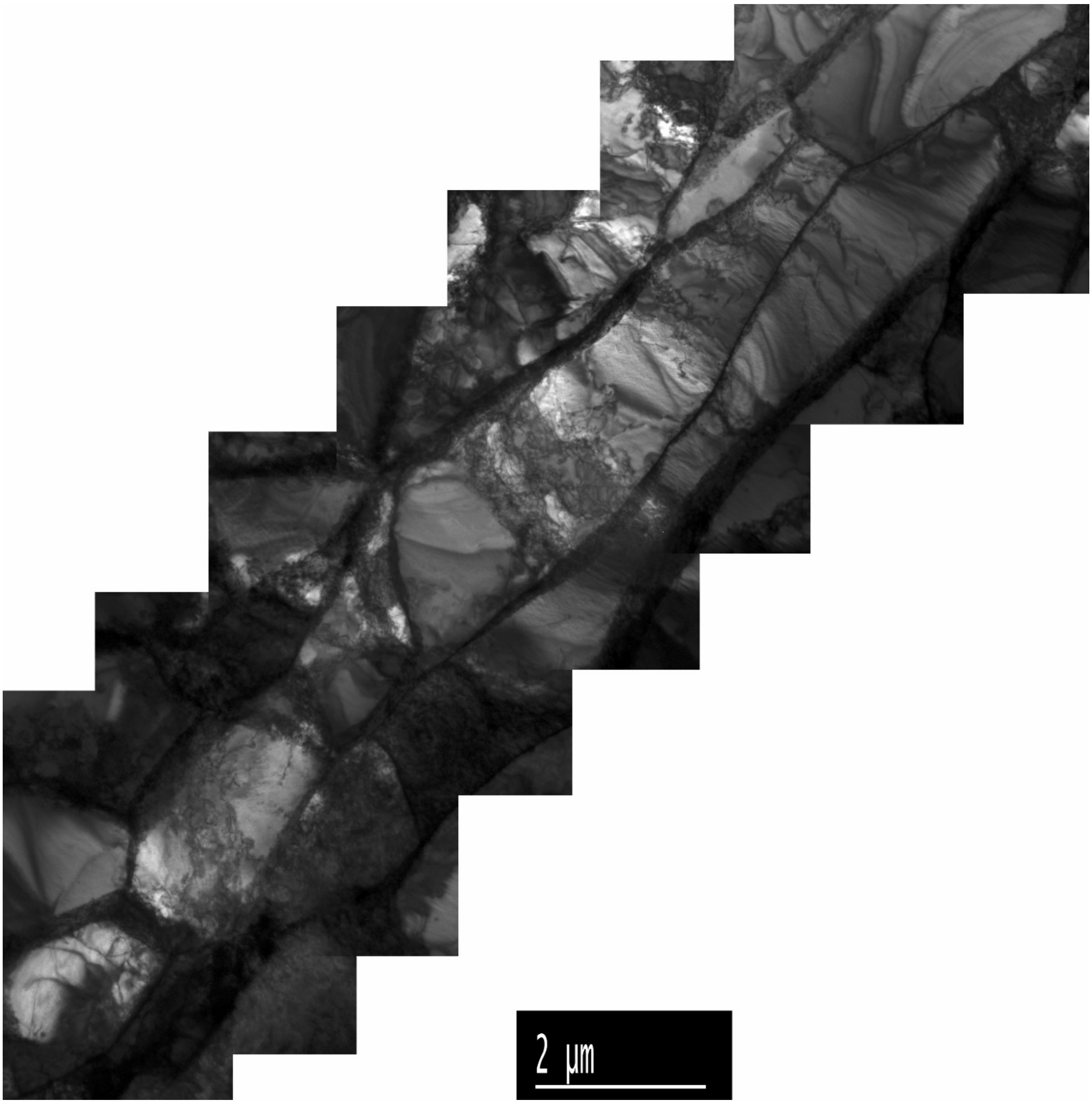

Fig.7. Composite TEM image of IGP after plastic deformation.

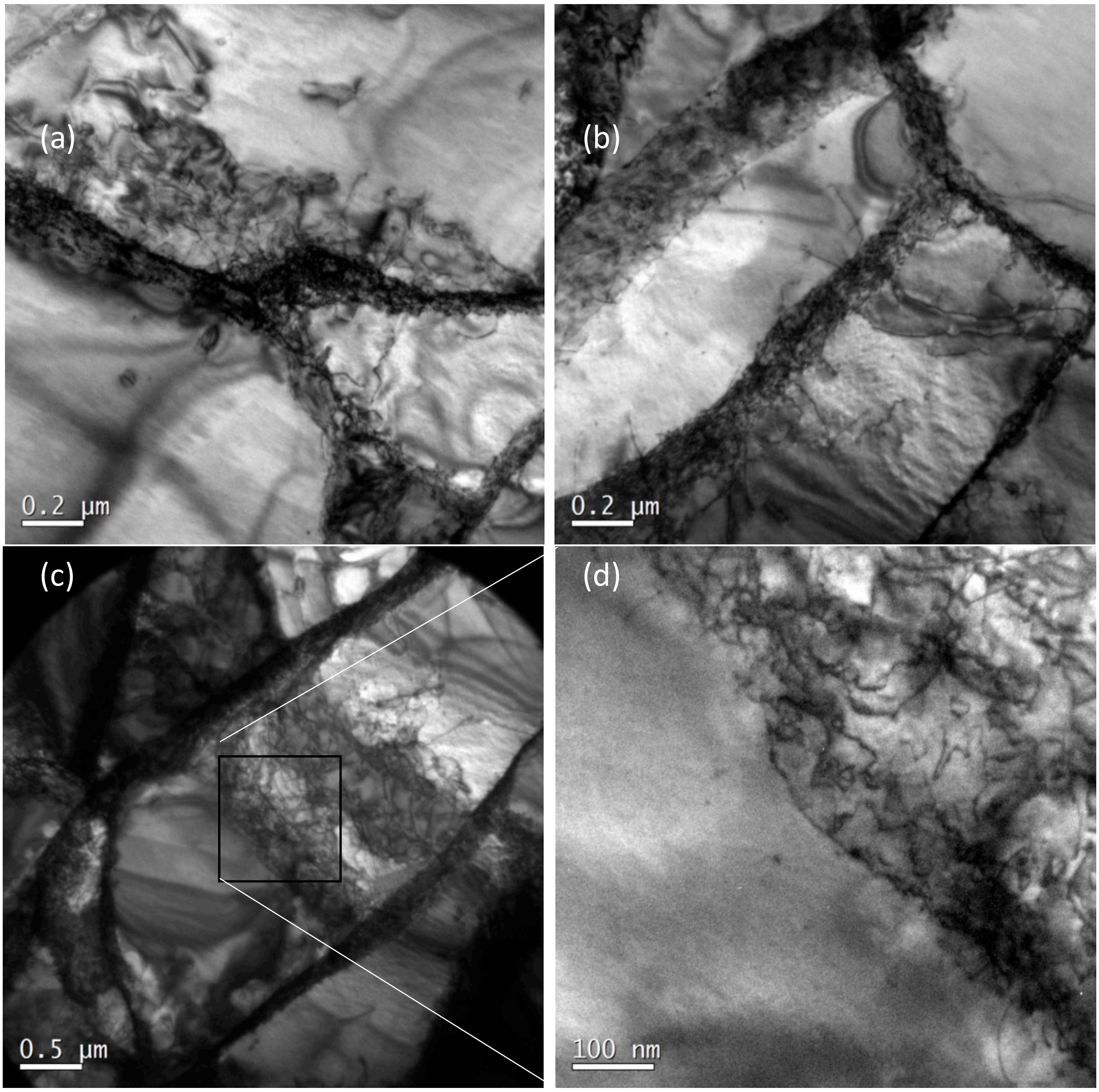

Fig.8. TEM images of IGP after plastic deformation.

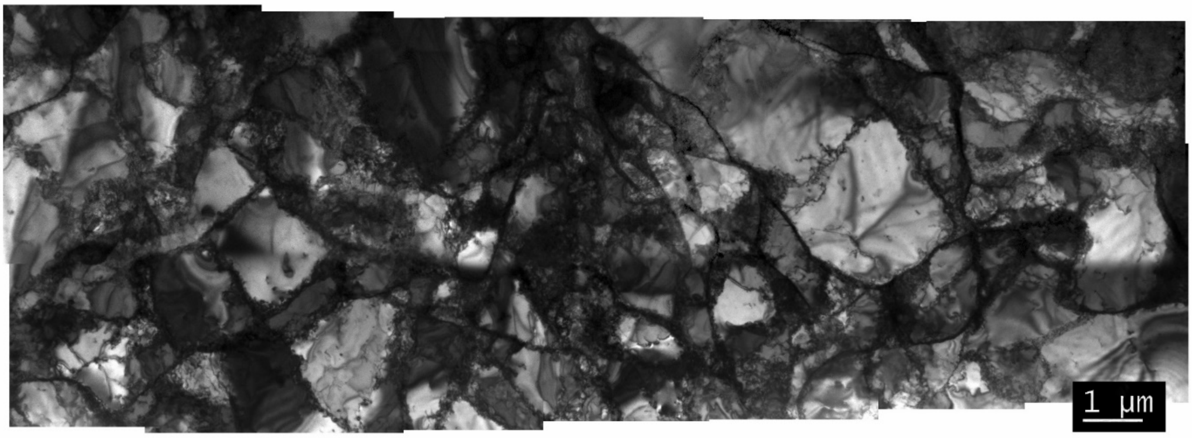

Fig.9. Composite TEM image of CFETR after plastic deformation.

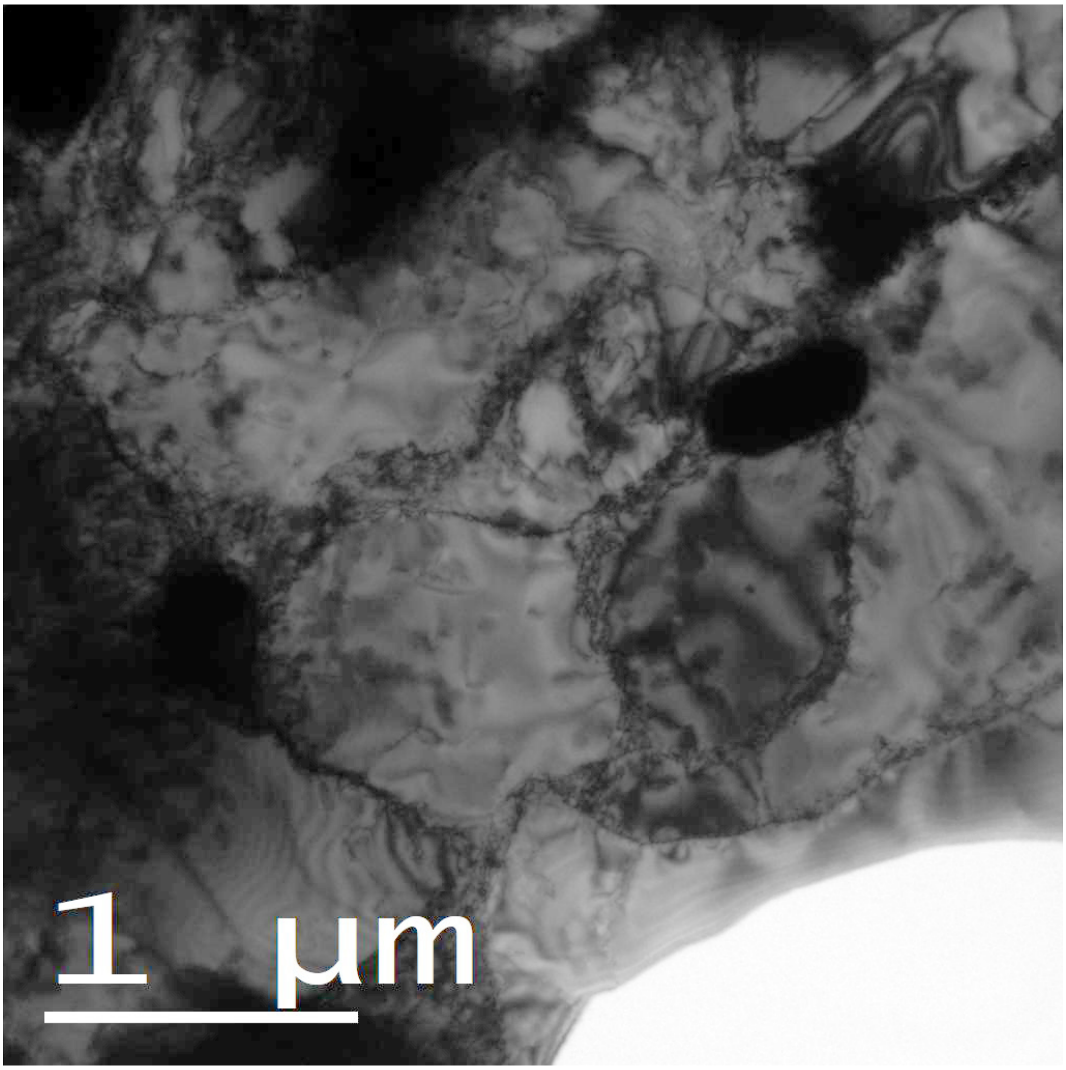

Fig.10. TEM images of W1TiC after plastic deformation.

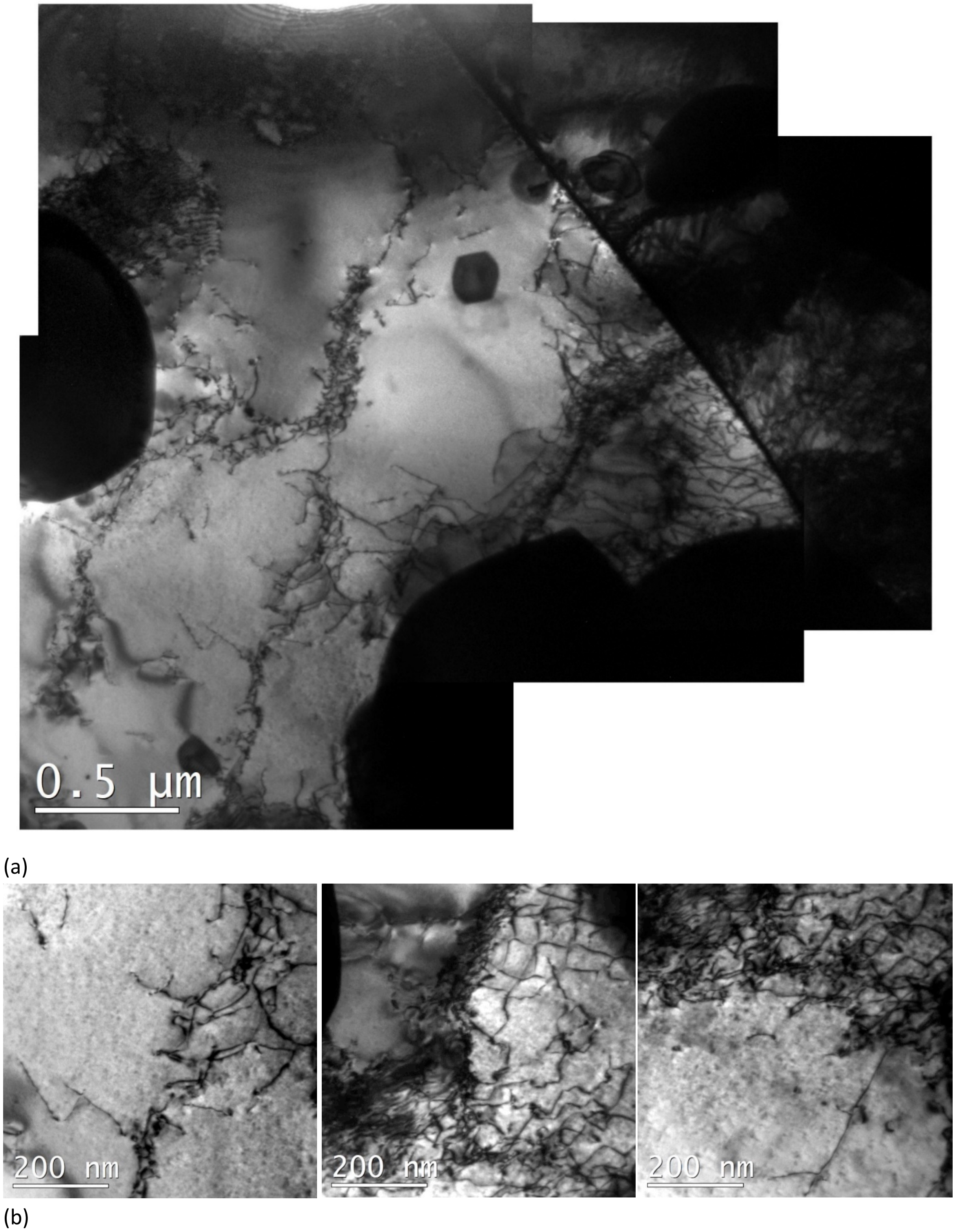
0.5 µm
(a)
200 nm
200 nm
200 nm
(b)

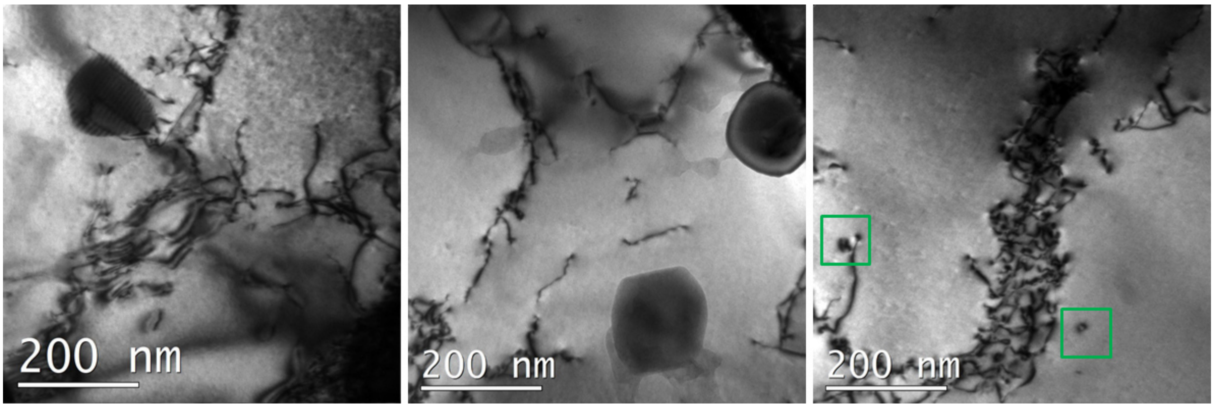

(c)

Fig.11. TEM images of W2YO after plastic deformation: (a) composite image; (b) high magnification images showing the region with low in the left image, high density in the middle image, and heterogeneous pattern of dislocations on the right image; (c) high magnification images showing the region containing Y_2O_3 precipitate near dislocation tangles in the left image, presence of Y_2O_3 precipitates isolated from the dislocation tangles/networks – middle image, and an example of dislocation loops observed after plastic deformation, see right image.

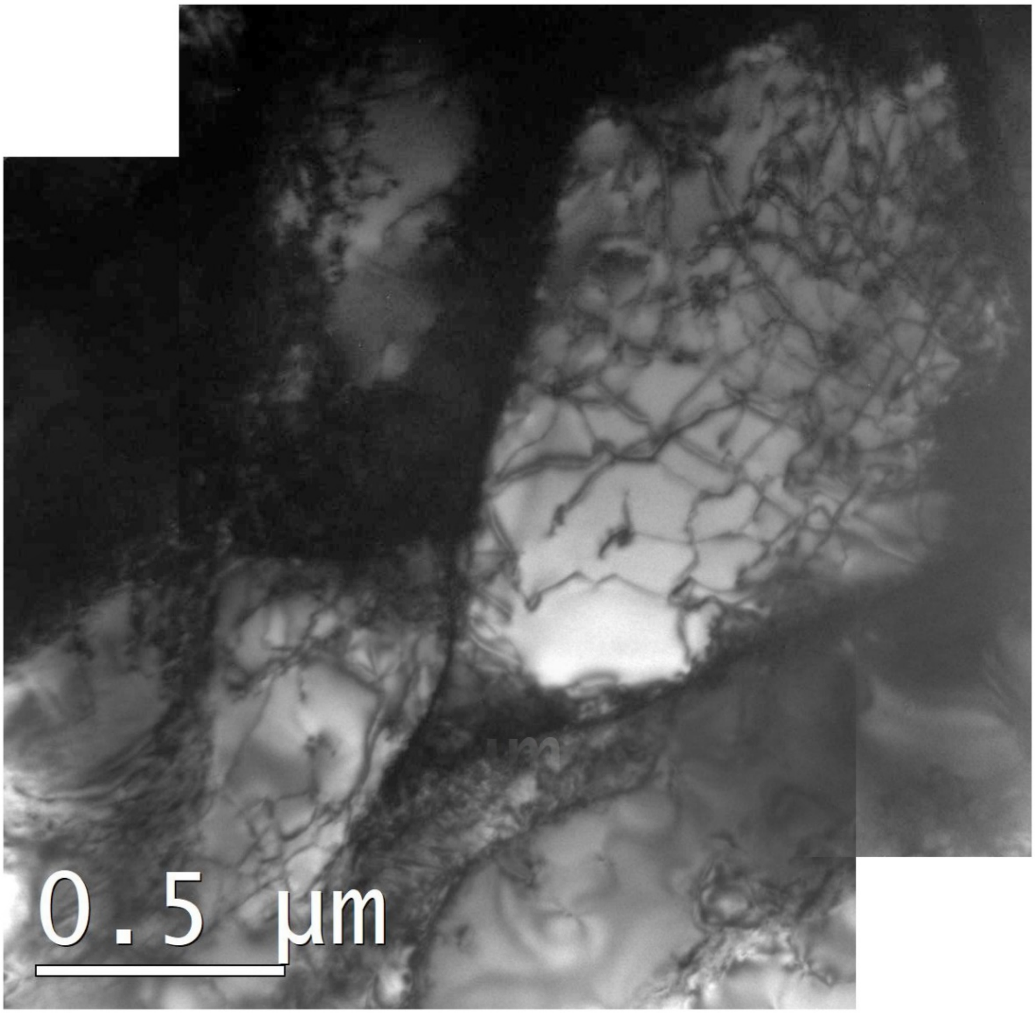

Fig.12. TEM images of FG after plastic deformation.

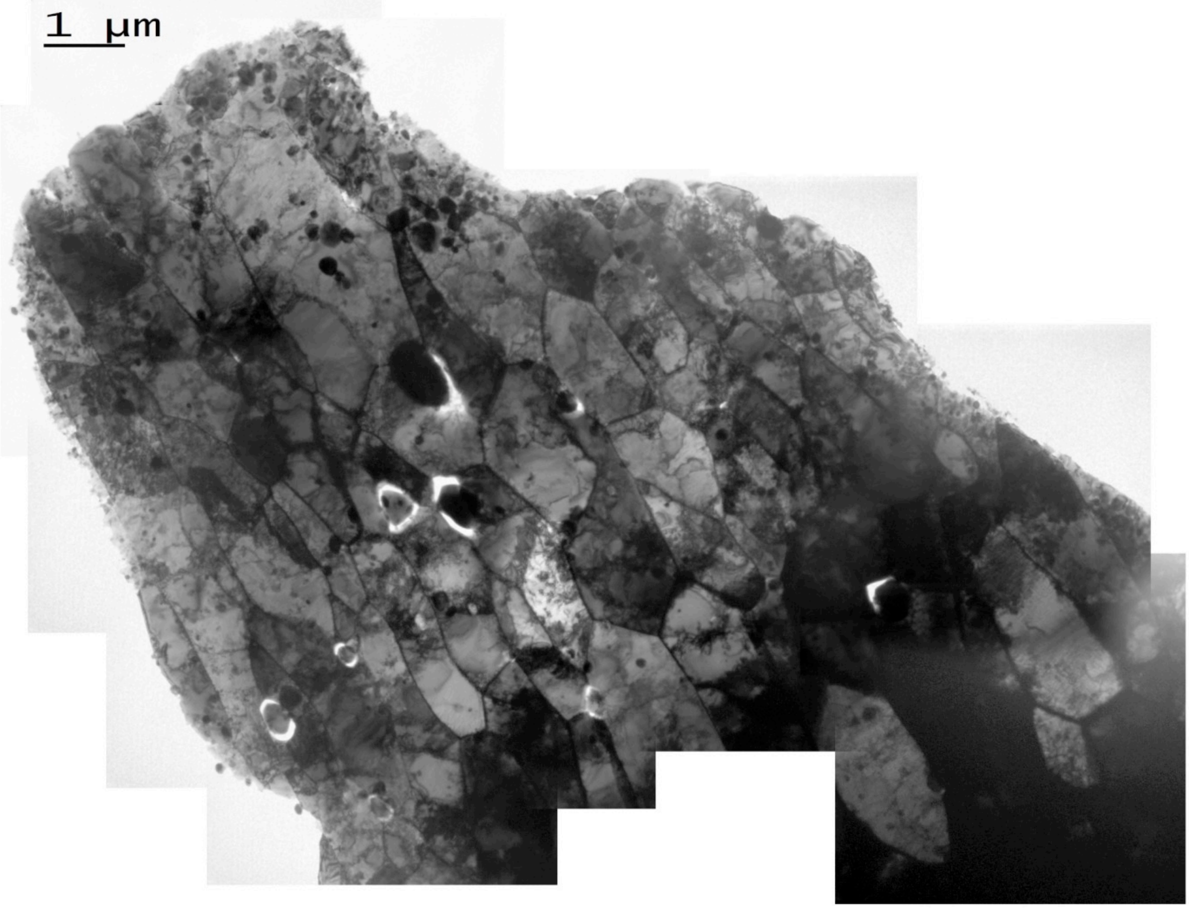

Fig.13. TEM images of W0.5ZrC after plastic deformation.

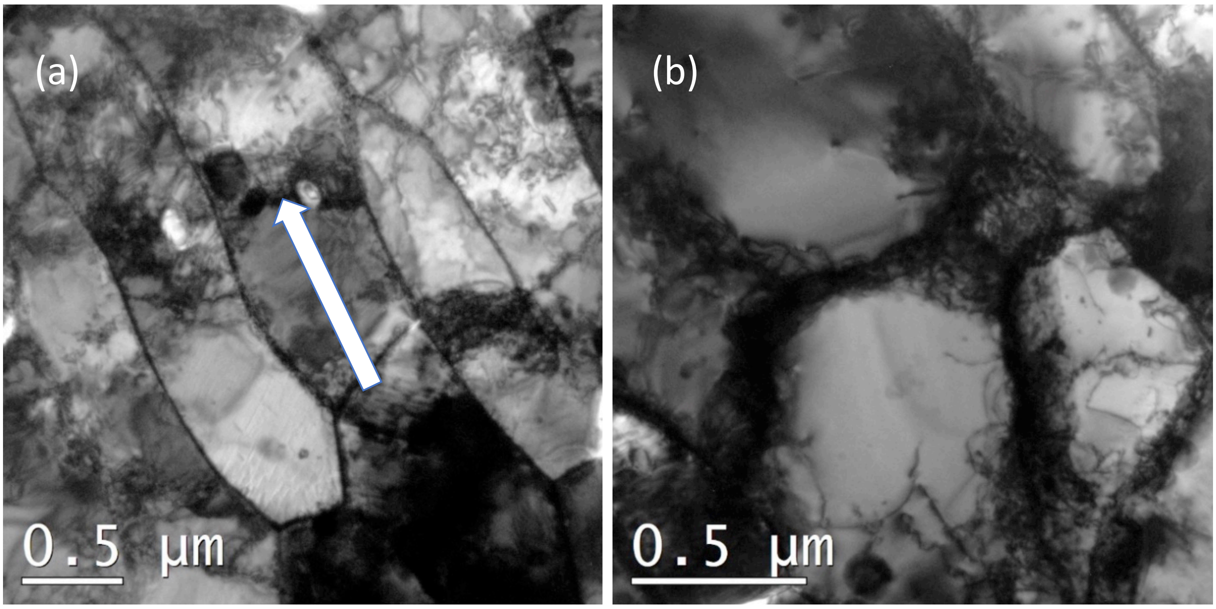

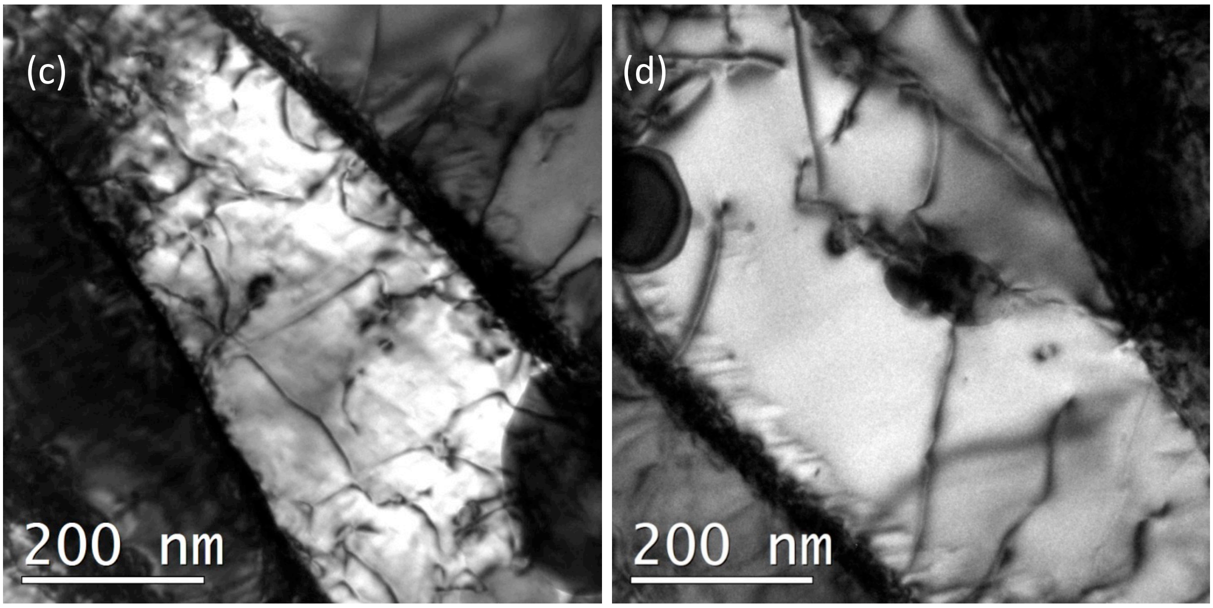

Fig.14. TEM images of W0.5ZrC after plastic deformation at 600°C showing: (a) morphology subgrains; (b) broadening of grain boundary interfaces; (c) patter of dislocations within a single sub-grain; (d) appearance of dislocations near ZrC precipitates.

6. Summary and concluding remarks

To summarize, we have studied parametrically the mechanical response of six tungsten products under tensile and bending deformation at 600°C. These tungsten grades were produced specifically for the nuclear fusion applications with a purpose of improving the operational temperature window by either reducing DBTT and/or increasing the recrystallization resistance. The selected materials are included in the currently running neutron irradiation programme, and therefore the obtained here data will serve as a reference dataset. The summary of mechanical and microstructural features is provided in Table 2.

The evolution of microstructure induced by plastic deformation at 600°C has been studied in detail by TEM using samples from the necking region of the tensile gauge section. Comparison of the reference microstructure and the one after 600C deformation provides a direct evidence on the microstructural evolution and mechanisms governing plastic deformation in the different W grades.

Table 2. Main characteristics of the microstructure and mechanical properties of the studied W grades.

Materials	**IGP**	**CFETR**	**FG**	**W1TiC**	**W2YO**	**W0.5ZC**
Composition	Pure W >99.97wt%	Pure W >99.94 wt%	Pure W >99.7 wt%)	99wt%W + 1wt% TiC	98wt%W + 2wt%Y_2O_3	99.5wt%W + 0.5wt%ZrC

Equivalent Medium Diameter (µm)	88.37	76.02	8.61	6.52	6.46	5.88
Initial dislocation density, m-2	4.5E+12	4.51E+12	1.05E+12	Not observed	2.36E+12	1.03E+13
Dislocation density after rupture at 600C, m-2	1.02E+14	2.07E+13	5.15E+13	7.65E+13	4.39E+13	5.51E+13
Hardness, 0.2 HV at RT	463 ± 10	506 ± 13	363 ± 10	492 ± 13	486 ± 18	542 ± 27
YS at 600C	477	538	321	428	392	642
UTS at 600C	490 ± 1	547 ± 34	458	610	507	679 ± 6
Uniform elongation at 600C	0	0	27	22	12	2 ± 1
Fracture strain × fracture stress at 600C	1170 ± 327	1093 ± 111	181	215	52	211 ± 26
Specific features of microstructure after plastic deformation at 600C	Dislocation loops with low density				Dislocation loops with low density	Dislocation loops with low density

On the basis of collected results and discussion provided in Section 3, the following statements can be made on the mechanical performance and microstructural evolution under deformation at 600°C:

(i) the highest tensile yield stress is acquired by W0.5ZrC alloy thanks to initially high dislocation density, small sub-grain size and high density of ZrC precipitates located at both: grain boundary interfaces and within grain interiors. PIM and FG materials exhibit the lowest yield stress, presumably due to very low initial dislocation density and absence of low-angle grain boundaries as strengthening units. On the other hand, the PIM and FG materials own very large uniform elongation and their ultimate tensile strength is comparable of higher than that of the commercial grades (IGP and CFETR). This suggests that the fracture toughness of the PIM and FG grades is expected to be rather high, however, the materials should be susceptible to the high cycle fatigue damage.

(ii) pure commercial W grades exhibit the largest fracture stress (~1.1 GPa) due to the very large reduction area. The fracture strength of other studied grades is much lower. This points to the fact that the accumulation of void damage, nucleation of micro-cracks and their coalescence occurs differently in the commercial pure W and advanced W-based alloys.

(iii) TEM analysis of the plastically deformed commercial pure W grades reveals very similar features of the microstructure, namely: presence of tangles and pile-ups near grain boundaries and broadening of grain boundaries structures, which points to the fact that grain boundaries are primary units resisting dislocation propagation. In the case of W1TiC and W2YO alloys, some dislocation tangles and pile-ups were also observed near the precipitates, demonstrating that these particles provide contribution to the strengthening of the material during the plastic deformation. The most homogeneous pattern of the dislocations after plastic deformation was seen in W0.5ZrC alloy – the material which had the most fine microstructural features (i.e. smallest sub-grain size, smallest precipitates and highest initial dislocation density) in the non-deformed state. It was also interesting to note the absence of any large pipe-ups or tangles near the ZrC precipitates after the deformation.

Following the above collected statements, we can see that the studied materials can be sub-divided into three groups: (i) pure commercial W products produced by powder metallurgy, subsequent forging and stress release; (ii) fine grain structure (PIM with Y_2O_3 and TiC particles, and FG) produced by powder injection molding or spark plasma sintering; (iii) fine grain structure W0.5ZrC produced by rolling and thermo-mechanical treatment. The particular differences between the precipitate-strengthened PIM and W0.5ZrC are: (i) much higher initial dislocation in the W0.5ZrC; (ii) much smaller size of ZrC precipitates in W0.5ZrC, and as a result of it – much higher coverage of grain boundary interfaces by these precipitates. The present assessment shows clearly that plastic deformation mechanisms under uniaxial tensile load differ in these three groups of materials. For further identification of possible material improvement, it is important to assess the mechanical response of these materials after neutron irradiation as well as to investigate the fracture toughness and fatigue properties in non-irradiated state, as this will provide a much broader picture of their expected performance during the operation under nuclear fusion environment expected in tokamaks.

Acknowledgements:

References:

[1] S.J. Zinkle, Advanced materials for fusion technology, Fusion Engineering and Design 74(1-4) (2005) 31-40.
[2] S.J. Zinkle, Fusion materials science: Overview of challenges and recent progress, Phys Plasmas 12(5) (2005) 058101.
[3] S. Matsuda, K. Tobita, Evolution of the ITER program and prospect for the next-step fusion DEMO reactors: status of the fusion energy R&D as ultimate source of energy, Journal of NUCLEAR SCIENCE and TECHNOLOGY 50(4) (2013) 321-345.
[4] M. Rieth, D. Armstrong, B. Dafferner, S. Heger, A. Hoffmann, M.-D. Hofmann, U. Jäntsch, Tungsten as a Structural Divertor Material, Advances in Science and Technology 73 (2010) 11-21.
[5] A. Giannattasio, Z. Yao, E. Tarleton, S.G. Roberts, Brittle–ductile transitions in polycrystalline tungsten, Philosophical Magazine 90 (2010) 3947-3959.
[6] R.H. Titran, J.R. Stephens, D.W. Petrasek, Refractory-Metal Alloys and Composites for Space Nuclear-Power Systems, Jom-J Min Met Mat S 40(7) (1988) A63-A63.
[7] G. Pintsuk, Tungsten as plasma facing material, Comprehensive Nuclear Materials 4 (2012) 551-581.
[8] M. Rieth, R. Doerner, A. Hasegawa, Y. Ueda, M. Wirtz, Behavior of tungsten under irradiation and plasma interaction, Journal of Nuclear Materials 519 (2019) 334-368.
[9] C. Linsmeier, M. Rieth, J. Aktaa, T. Chikada, A. Hoffmann, J. Hoffmann, A. Houben, H. Kurishita, X. Jin, M. Li, A. Litnovsky, S. Matsuo, A. von Muller, V. Nikolic, T. Palacios, R. Pippan, D. Qu, J. Reiser, J. Riesch, T. Shikama, R. Stieglitz, T. Weber, S. Wurster, J.H. You, Z. Zhou, Development of advanced high heat flux and plasma-facing materials, Nuclear Fusion 57(9) (2017).
[10] H. Noto, S. Taniguchi, H. Kurishita, S. Matsuo, T. Ukita, K. Tokunaga, A. Kimura, Effect of grain orientation and heat treatment on mechanical properties of pure W, Journal of Nuclear Materials 455(1-3) (2014) 475-479.
[11] H. Sheng, G. Van Oost, E. Zhurkin, D. Terentyev, V.I. Dubinko, I. Uytdenhouwen, J. Vleugels, High temperature strain hardening behavior in double forged and potassium doped tungsten, Journal of Nuclear Materials 444(1-3) (2014) 214-219.
[12] G. Pintsuk, I. Uytdenhouwen, Thermo-mechanical and thermal shock characterization of potassium doped tungsten, Int J Refract Met H 28(6) (2010) 661-668.
[13] B. Gludovatz, S. Wurster, A. Hoffmann, R. Pippan, Fracture toughness of polycrystalline tungsten alloys, Int J Refract Met H 28(6) (2010) 674-678.
[14] J. Reiser, S. Wurster, J. Hoffmann, S. Bonk, C. Bonnekoh, D. Kiener, R. Pippan, A. Hoffmann, M. Rieth, Ductilisation of tungsten (W) through cold-rolling: R-curve behaviour, Int J Refract Met H 58 (2016) 22-33.
[15] S. Wurster, R. Pippan, Miniaturized Cantilever Bending Experiments for Determination of Fracture Properties of Tungsten as a Model Material, Determination of Mechanical Properties of Materials by Small Punch and Other Miniature Testing Techniques, 2nd International Conference Sstt (2012) 271-275.
[16] J.W. Coenen, S. Antusch, M. Aumann, W. Biel, J. Du, J. Engels, S. Heuer, A. Houben, T. Hoeschen, B. Jasper, F. Koch, J. Linke, A. Litnovsky, Y. Mao, R. Neu, G. Pintsuk, J. Riesch, M. Rasinski, J. Reiser, M. Rieth, A. Terra, B. Unterberg, T. Weber, T. Wegener, J.H. You, C. Linsmeier, Materials for DEMO and reactor applications-boundary conditions and new concepts, Physica Scripta T167 (2016).
[17] M. Rieth, e. al., A brief summary of the progress on the EFDA tungsten materials program, Journal of Nuclear Materials 442(1-3) (2013) S173-S180.
[18] J. Riesch, Y. Han, J. Almanstotter, J.W. Coenen, T. Hoschen, B. Jasper, P. Zhao, C. Linsmeier, R. Neu, Development of tungsten fibre-reinforced tungsten composites towards their use in DEMO-potassium doped tungsten wire, Physica Scripta T167 (2016).

[19] L.H. Zhang, Y. Jiang, Q.F. Fang, Z.M. Xie, S. Miao, L.F. Zeng, T. Zhang, X.P. Wang, C.S. Liu, Microstructure and mechanical properties of tungsten composite reinforced by fibre network, Front Mater Sci 11(2) (2017) 190-196.
[20] Z.M. Xie, R. Liu, S. Miao, X.D. Yang, T. Zhang, X.P. Wang, Q.F. Fang, C.S. Liu, G.N. Luo, Y.Y. Lian, X. Liu, Extraordinary high ductility/strength of the interface designed bulk W-ZrC alloy plate at relatively low temperature, Sci Rep-Uk 5 (2015).
[21] D.H. Lassila, F. Magness, D. Freeman, Ductile-Brittle Transition Temperature testing of tungsten using the three-point bend test, Lawrence Livermore National Lab., CA (United States), 1991.
[22] G. Pintsuk, E. Diegele, S.L. Dudarev, M. Gorley, J. Henry, J. Reiser, M. Rieth, European materials development: Results and perspective, Fusion Engineering and Design 146 (2019) 1300-1307.
[23] S. Antusch, D. Armstrong, B. Britton, L. Commin, J. Gibson, H. Greuner, J. Hoffmann, W. Knabl, G. Pintsuk, M. Rieth, S. Robert, T. Weingaertner, Mechanical and microstructural investigations of tungsten and doped tungsten materials produced via powder injection molding, Nuclear Materials and Energy 3-4 (2015) 22-31.
[24] S. Heuer, J. Matejicek, M. Vilemova, M. Koller, K. Illkova, J. Veverka, T. Weber, G. Pintsuk, J.W. Coenen, C. Linsmeier, Atmospheric plasma spraying of functionally graded steel/tungsten layers for the first wall of future fusion reactors, Surf Coat Tech 366 (2019) 170-178.
[25] ASTM, Standard Test Methods for Bend Testing of Material for Ductility, E290-14, ASTM international, 2014.
[26] C. Yin, D. Terentyev, T. Pardoen, A. Bakaeva, R. Petrov, S. Antusch, M. Rieth, M. Vilemova, J. Matejicek, T. Zhang, Tensile properties of baseline and advanced tungsten grades for fusion applications, Int J Refract Met H 75 (2018) 153-162.
[27] P. Hirsch, A. Howie, R. Nicholson, D.W. Pashley, M.J. Whelan, Microscopy of Thin Crystals, Krieger Publishing Company Malabar, Florida1977.
[28] D. Terentyev, M. Vilemova, C. Yin, J. Veverka, A. Dubinko, J. Matejicek, Assessment of mechanical properties of SPS-produced tungsten including effect of neutron irradiation, International Journal of Refractory Metals and Hard Materials 89 (2020) 105207.
[29] A. Dubinko, D. Terentyev, A. Bakaeva, K. Verbeken, M. Wirtz, M. Hernandez-Mayoral, Evolution of plastic deformation in heavily deformed and recrystallized tungsten of ITER specification studied by TEM, Int. Journal of Refractory Metals and Hard Materials 66 (2017) 105-115.